

An Unsupervised Deep XAI Framework for Localization of Concurrent Replay Attacks in Nuclear Reactor Signals

Konstantinos Vasili*, Zachery T. Dahm, William Richards, Stylianos Chatzidakis

Affiliation: School of Nuclear Engineering, Purdue University, West Lafayette, IN 47907

***Corresponding author:** vasilik@purdue.edu

Abstract

Next generation advanced nuclear reactors are expected to be smaller both in size and power output, relying extensively on fully digital instrumentation and control systems. These reactors will generate a large flow of information in the form of multivariate time series data, conveying simultaneously various non-linear cyber-physical, process, control, sensor, and operational states. Ensuring data integrity against deception attacks is becoming more and more important for networked communication cyber-physical control systems and a requirement for safe and reliable operation. Current efforts to address replay attacks, a special kind of deception cyber event, almost universally focus on watermarking or supervised anomaly detection approaches without further identifying and characterizing the root cause of the anomaly. In addition, these approaches rely mostly on synthetic data with uncorrelated Gaussian process and measurement noise and full state feedback or are limited to univariate signals, signal stationarity, linear quadratic regulators, or other linear-time invariant state-space which may fail to capture any unmodeled system dynamics. In the realm of regulated nuclear cyber-physical systems, additional work is needed on characterization of replay attacks and explainability of predictions using real data. Here, we propose an unsupervised explainable AI (XAI) framework based on a combination of autoencoder and customized windowSHAP algorithm to fully characterize real-time replay attacks, i.e., detection, source identification, timing and type, of increasing complexity during a dynamic time evolving reactor process. The proposed XAI framework was benchmarked on several real-world datasets from Purdue's nuclear reactor PUR-1 with up to six signals concurrently being replayed. In all use cases, the XAI framework was able to detect and identify the source and number of signals being replayed and the duration of the falsification with 95% or better accuracy.

Keywords: replay attack, autoencoders, explainable AI, PUR-1, multivariate time series data, windowSHAP

Introduction

Currently, there is a growing trend in the nuclear industry toward advanced reactor designs such as microreactors and small modular reactors. To make these designs cost competitive and operationally flexible, digital instrumentation and control, further supported by wired or wireless communication networks will need to be implemented. These systems promise centralized or semi-autonomous control, real time monitoring, prognostics, diagnostics, or unattended operation [1][2][3][4]. Despite the numerous advantages of digital instrumentation and control, new challenges emerge including the near impossibility of maintaining constant human surveillance over potential anomalies or cyber events within the digital system [5]. Unlike conventional information technology (IT) systems where the main focus is the protection of network data, cyber events on critical, networked control infrastructure could affect not only the data but physical and control processes through a variety of different ways and may cause economic loss, (e.g., due to unnecessary shutdown of the reactor) or equipment damage [6] [7]. It is worth noting the infamous Stuxnet malware detected in 2010, which affected the digitized industrial control system of a nuclear facility [8] [9] along with other non-nuclear facilities around the world.

Teixeira et al. [6] present an overview of cyber events that could compromise control systems and define a 3-dimensional cyber physical attack space comprised of knowledge, disclosure, and disruption resources. The main properties of an attack include violation of data confidentiality, integrity, and availability. Characteristic example of data availability violation is a Denial of Service (DoS) [10] [11] where an adversary prevents the data from reaching their destination. Examples of data integrity violation are deception attacks which include False Data Injection (FDI) [12] [13] or replay attacks [14] [15]. FDI attacks have received attention recently and a review of state-of-the art against modern power systems can be found in [16]. A replay attack, a subset of deception threat, requires the adversary to deploy disclosure and disruption resources but does not require prior system knowledge making it particularly concerning and difficult to detect due to its simplicity and effectiveness. During a replay attack, the adversary intercepts an unknown amount of information which resends at a later time with the goal of deceiving the operators [6], [15]. Contrary to an FDI attack which may inject conceptually erroneous data into the system, a replay attack resends valid data from a past operational mode making it harder to detect and flag as an anomaly. During Stuxnet, though not primarily a replay attack, recorded normal data were replayed to the monitoring system to create the illusion that the system was operating normally, while an even more sophisticated attack was ongoing.

Over the past years, several techniques have been proposed for identifying anomalies as a result of replay attacks including watermarking [14] [15] [17] [18] and data driven approaches [18] [19]. In one of the earliest work in the field, Mo and Sinopoli, 2009 [14] investigated a discrete, linear time invariant, Gaussian control system for anomaly detection. They proved that the difference between the actual and the predicted measurements from a Kalman filter follows a Gaussian distribution. Subsequently, a χ^2

failure detector was used to perform intrusion detection by adding random noise to the signal and then comparing the difference with a threshold in a predefined window length. Yao and Smidts, 2020 [15] extended this approach by adding a second χ^2 detector to include classification of the anomaly into FDI or other anomaly. While successful, both studies relied on linearized mathematical models, uncorrelated Gaussian noise, and required specific parameterizations to reflect the system non-linear dynamics. In addition, signal stationarity was assumed, and synthetic data were used for proof of concept.

Data driven techniques have also been proposed for detection of anomalies as a result of replay attacks in a variety of different domains, including smart cities and industrial control systems. AA Elsaedy et al. (2020) developed a Deep Learning (DL) pipeline for detecting anomalies in smart cities [19]. A multi-sensor infrastructure was designed to collect multivariate data and then different DL architectures, including Convolutional Neural Networks (CNNs), were trained as a binary classification problem to classify the time series into normal or attack. Of relevance to our work, Gargoum et al. [20] propose a data driven, two stage framework for anomaly detection and verification. The approach combines matrix profile-based change-point detection followed by a convLSTM architecture for distinguishing normal from replayed sensor measurements. The framework introduces spatio-temporal features to subsequences of the time series flagged as a replay attack to verify the detection. Despite its novelty, the method appears to be applied to a single feature and does not address scenarios involving multi-sensory or multivariate environments where replay attacks may target any arbitrary signal combination. Furthermore, even if separate frameworks were deployed to monitor each signal, the approach would fail in scenarios where the anomaly is contextual, flagged by the absence of expected inter-signal correlations rather than deviations in individual signal patterns.

Wang et al. [21] explored an LSTM framework for predicting and detecting FDI and replay attack in multivariate times series (MTS) data of an industrial control process. The framework successfully identified replayed sequences by comparing the prediction with a predefined prediction error. However, the framework considered a scenario where all the signals are falsified creating clearly distinguishable patterns while not able to identify specific signals or duration and time of attack. To address this, Dahm et al., 2025 [22] extended this approach by adding interpretability to an LSTM predictive framework for replay attack scenarios in MTS data from PUR-1 nuclear reactor. The framework, successfully demonstrated using real data from PUR-1, identified nonstationary, concurrent replay attack scenarios of increasing complexity by extracting Shapley values that interpret the difference between a critical signal prediction and the actual signal value. Despite its success, the framework relies on the prediction of a single critical signal not known a priori to the adversary, which limits its applicability in scenarios where the critical signal is itself the target of a possible attack. Other approaches are proposing clustering based statistical methods [23] [24] and classical ML approaches such as SVM [25]. Although suitable for their specific

application, these approaches do not consider the time component and therefore are not suitable for real time monitoring.

Replay attacks, as a specific subclass of cyber threats, fall into the general field of anomaly detection. With advancements in computational units observed in the last years, significant attention is dedicated to anomaly detection using AI/ML. A comprehensive review is listed in this survey [26]. Among various approaches, unsupervised methods using Autoencoders (AE) have shown strong performance, especially in cases where abnormal events are rare. A promising research direction explores the combination of AE with SHAP (Shapley Additive exPlanations) analysis to provide interpretable insights into the deviation from the normal patterns [27] [28] [29]. However, despite the significance when dealing with time evolving critical processes, the absence of the time dimension in SHAP analysis combined with deeper architectures has not been given proper attention. In this work, we aim to fill this gap by combining and expanding two individually proven techniques, into a unified, robust, and efficient framework. We use a deep unsupervised encoder-decoder architecture which combined with a modified Explainable AI (XAI) module allows for real-time reconstruction error analysis and characterization of signal-level replay attack scenarios of increased complexity during a dynamic, and time evolving reactor operation. The framework extends beyond a binary classification task by quantifying feature importance in time and feature space. It identifies a general condition which triggers a deviation from expected reactor behavior and then further investigates the contribution of each signal by calculating Shapley values in the time and feature space. The proposed approach was benchmarked against real-world reactor data from Purdue's nuclear reactor (PUR-1) and can be extended to any control system with predictable operational modes.

Use case

Scenario

The use case involves injecting multiple replay attacks in different sensors with data recorded from a past steady state condition. This is to experimentally simulate an adversary aiming to deceive an operator that the system remains at high power during a shutdown process. The event starts when the SCRAM button is activated. This cuts the magnet current to the control rods, which are then rapidly inserted in the reactor core. The control rods are made of neutron absorbing material and immediately terminate the reactor heat production process. From that point the reactor power is due to generated residual heat from precursor concentrations. In a normal process the sensor readings, after visualized, will depict a rapidly changing condition as shown in Figure 1 (left). The conceptual cyber scenario is shown in Figure 1 (right), where the green line depicts the SCRAM button activation, the red line represents the expected response, and the blue line shows the observed behavior due to the cyber event.

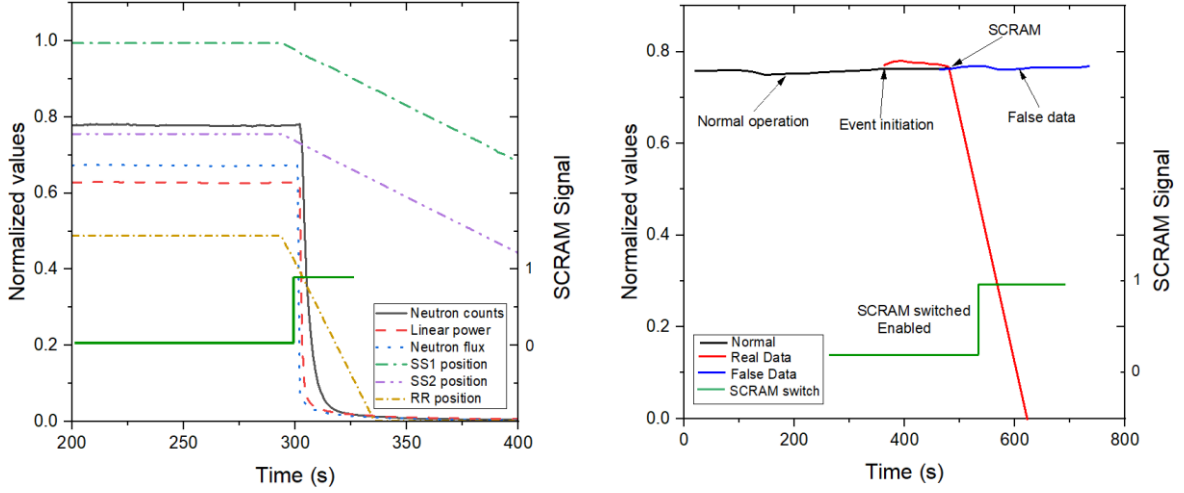


Figure 1: Variation in neutron counts after a forced shutdown (SCRAM) (left). Event initiation represented by the blue line where the SCRAM event is not followed by decreasing values (right).

To explore the efficiency of the proposed framework on the scenario, replay attack events of increasing complexity were experimentally simulated. A set of n sensor measurements taken from a control system, can be described as time series data in the following form:

$$X(t) = [x_1(t), x_2(t), \dots, x_n(t)]$$

Where each element $x_i(t)$ represents the reading from the i -th sensor at time t . Under the assumption that the attacker has access to the system, the attacker performs a replay attack in two stages as described in relevant literature [20], [38]. In the first stage the system is intercepted and a k unknown number of signals for an unknown time interval I is recorded. The recorded set can be represented as:

$$\tilde{X}(t) = [\tilde{x}_1(t), \tilde{x}_2(t), \dots, \tilde{x}_k(t)], \quad t \in I$$

The time interval I is denoted as: $I = [t_{start}, t_{start} + T]$,

Where t_{start} , is the start of the recording and T is the period of the recorded signal.

In the second stage, the attacker injects the recorded set \tilde{X} at a later time interval denoted as: $I_{attack} = [t_{attack}, t_{attack} + NT]$, where t_{attack} represents the attack start time and N represents the number of times the recorded set is repeated. If $N = 1$, the attack can be regarded as a delay attack. For our use case k starts with one and increases to six signals: neutron counts (ch.1), reactor power (ch. 3), neutron flux (ch. 4), the regulatory rod (rr-position), the SS1 rod, and the SS2 rod. It is assumed that these signals will be primarily a target for a cyber-attack event, since these are typically monitored by operators on the control console. The recorded time interval I is selected during a steady state condition before the SCRAM event. The period T is set equal to 20 seconds of steady state operation, t_{attack} is set just after the SCRAM button is pressed, which is around 300 s, and N is set equal to 5, creating 100 seconds of replayed signals covering

the entire SCRAM event (Figure 2). The selection of the above parameters (timing, period and number of signals) can lead to different effects, creating different attack scenarios which may mislead the operator regarding the true reactor condition. Depending on the actions that the operator decides to follow, the potential damage may include huge economic losses or even human loss, therefore the significance of correctly and timely identifying the replay attack is evident. After the attack, all the signals return to their normal values, which are small sensor values due to the large negative reactivity inserted by the control rods.

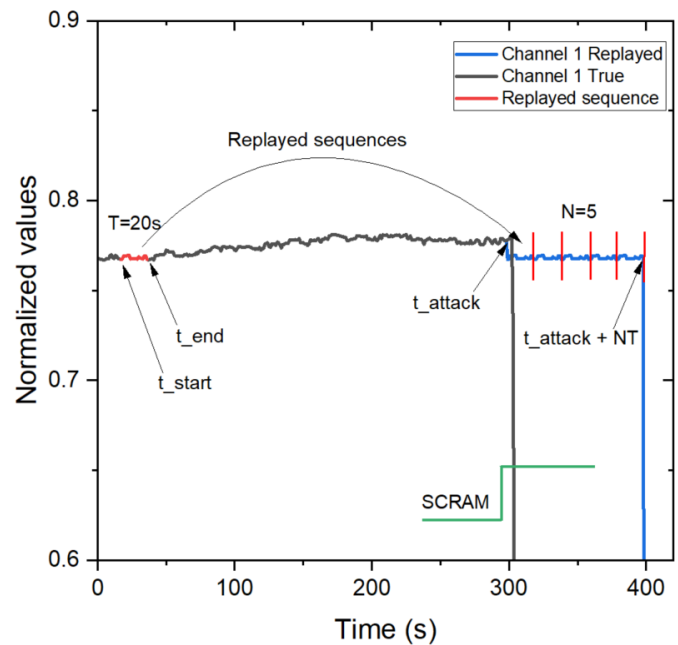


Figure 2: Replay attack scenario for Channel 1. By applying the same process to additional signals, concurrent replay attacks of increasing complexity are simulated.

In Figure 1, it is noted that although in actuality the insertion of the control rods is immediate into the reactor's core, in the course of a few seconds, the rr rod is immediately seen to insert the core, while the SS1 and SS2 are shown to last around 300 seconds until fully inserted. This is more due to the drivers of the control rods rather than the actual rod movements, creating a unique pattern which helps the reactor operator to identify a SCRAM process in his console.

PUR-1

Real reactor datasets cannot be easily found in the literature and most of the work reported in the nuclear domain relies on simulated or synthetic data with limited physical or artificial inconsistencies, e.g., noise, null values and outliers, making the dataset near perfect for data-driven testing [30] [31] [32] [33] [34]. Here, we leverage Purdue's University research reactor PUR-1 (Figure 3) [35] [36]. PUR-1 is a pool-type

reactor licensed to operate up to 10 kWth continuous power, and the only reactor in the United States with a fully digital instrumentation and control system, which allows for real time access to data and remote monitoring. A digital twin [37] is enabling data collection of more than 2000 parameters per sampling frequency, in real time via a monitoring workstation (Figure 3).

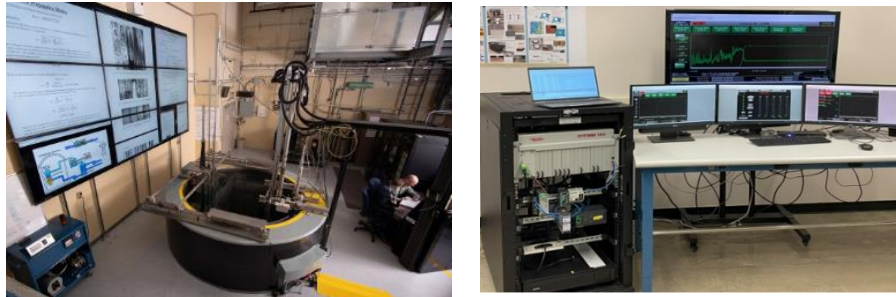


Figure 3: PUR-1 facility (left). Digital twin away from reactor building with no direct line of sight (right).

PUR-1 is only one component of a cyber-physical system which consists of five layers (Figure 4) [36]. Layers 0 to 3 are located inside the PUR-1 facility, and Layer 4 is located in a different building with no direct line of sight to the reactor facility. The reactor operation dynamics can be regarded as a multidimensional temporal sequence of sensor readings which are generated from Layers 0 to 3.

A fundamental requirement for any cyber event including FDI and replay attacks lies in the intruder’s ability to have gained access to the network. For our use case, we assume that the intruder has *a priori* system access down to Layer 1 (but not to Layer 0) and consequently is able to record signals of interest and replay them at a later time.

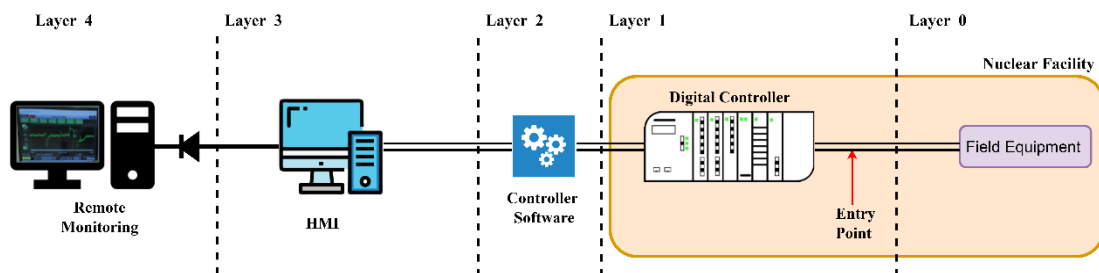


Figure 4: Cyber physical system architecture for PUR-1 cybersecurity testing.

Figure 5 presents the architecture that was developed to inject replay attacks and collect falsified data [36]. The architecture consists of two sections: (i) the Remote Location (left), where an attacker’s PC connects to the monitoring workstation via a network switch to enable the injection of false data; and (ii) the Control Room (right), which hosts the real-time reactor data network, including controllers, sensors, human-machine interfaces (HMIs), operational processes, and incoming signals used for decision-making [22] [36].

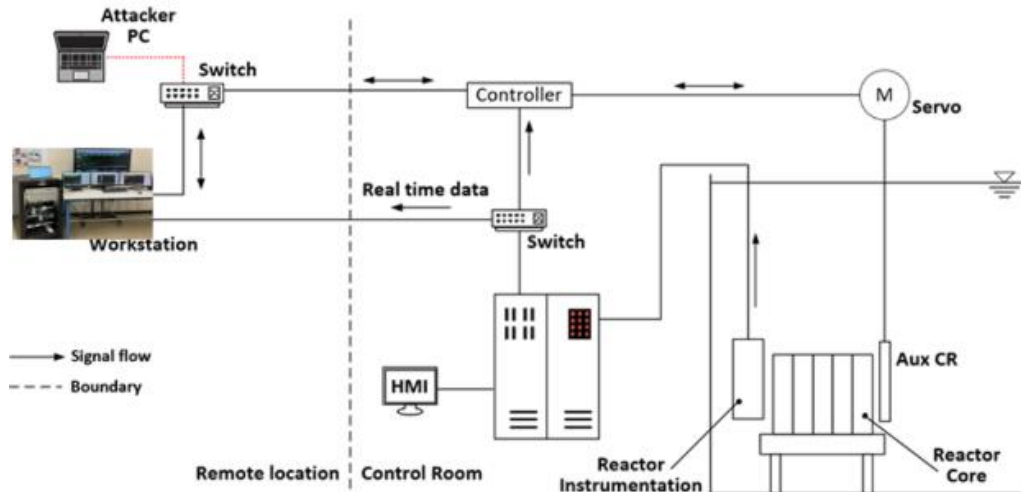


Figure 5: Architecture for injecting false data.

Data

The data are extracted from the digital twin workstation (Figure 3) in tabular format capturing either all or a subset of the available signals. Each row corresponds to a sampling frequency of one second, with columns representing different signals, forming a MTS dataset that reflects the reactor operational condition at each recorded time step. The high dimensionality, which contains over 2,000 signals, leads to increased computational costs and potential performance concerns, therefore, a reduction in the signal number used for the training of the models is needed. We identified and selected nine key signals that most accurately represent the reactor's functionality. The selected signals are shown in Table 1.

The collected operational data are subject to various artifacts such as fluctuations, outliers, null values, and noise. These inconsistencies arise due to several factors including limitations or imperfections in the data collection instruments, and the inherent complexity of the monitoring system. In addition, human operation and decision-making behaviors contribute with variability, as each operator may handle the reactor differently at same occasions, which is reflected in the recorded data. The frequency and nature of these artifacts can vary depending on the reactor's operational mode, whether in shutdown or any other active operation.

Table 1: Signals used for the training, testing and falsification

Feature	Units	Description
Neutron counts	1/s	Neutron counts per second as measured by channel 1
Linear power	%	Reactor power as measured by channel 3
Neutron flux	%	Neutron flux as measured by channel 4
ss1-position	cm	Distance an electromagnet has removed SS1 from the core
ss2-position	cm	Distance an electromagnet has removed SS2 from the core
rr-position	cm	Distance an electromagnet has removed RR from the core
rr-active-state	-	Categorical with three discrete values (insert-withdraw-steady)
ss1-active-state	-	Categorical with three discrete values (insert-withdraw-steady)
ss2-active-state	-	Categorical with three discrete values (insert-withdraw-steady)

47 datasets of full power cycles were collected and used for the initial training of the algorithms. Each dataset contains reactor operation of around 5700 seconds or 1.5 hours, from start up to shutdown including transient and steady state conditions at different power levels (Figure 6). Additionally, a collection of 24 SCRAM datasets of around 800 seconds each was used, showing the SCRAM event at various power levels (Figure 7).

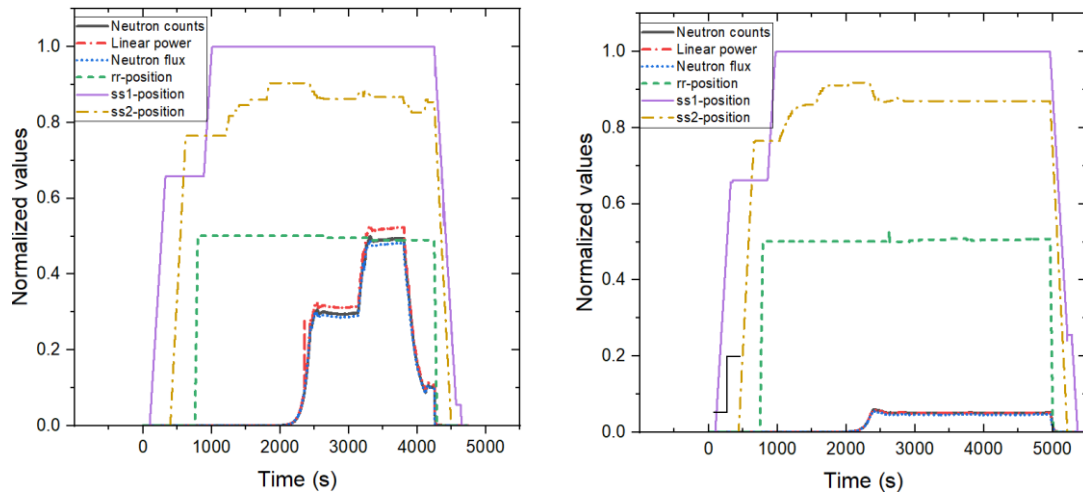


Figure 6: Examples of signal values variation in different full power cycles of PUR-1 operation

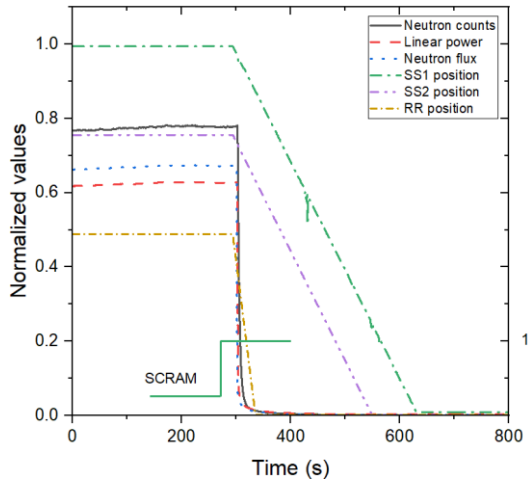
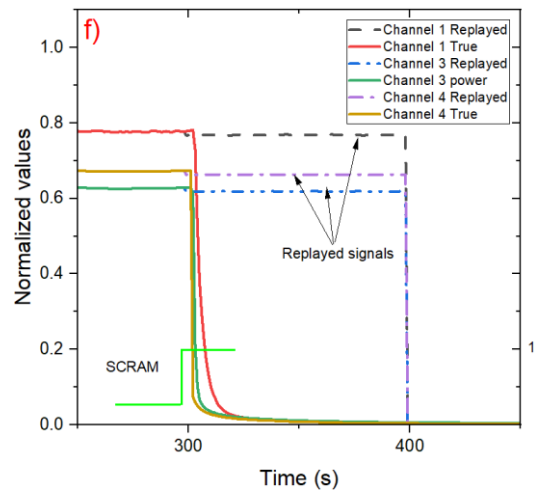
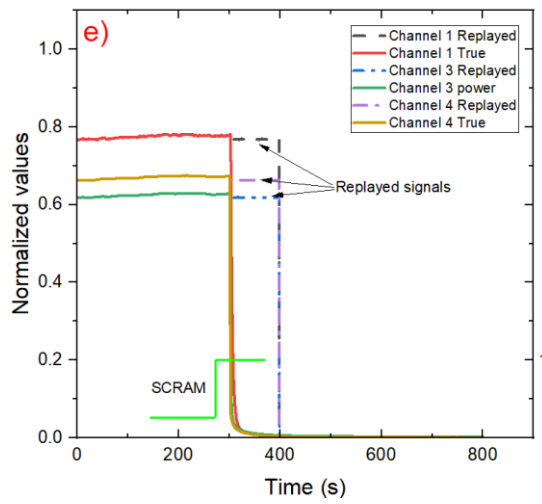
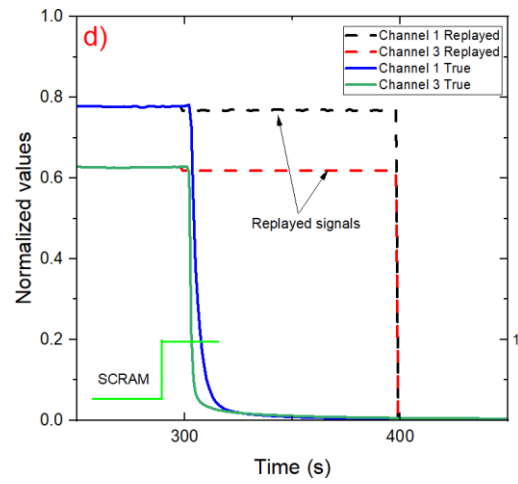
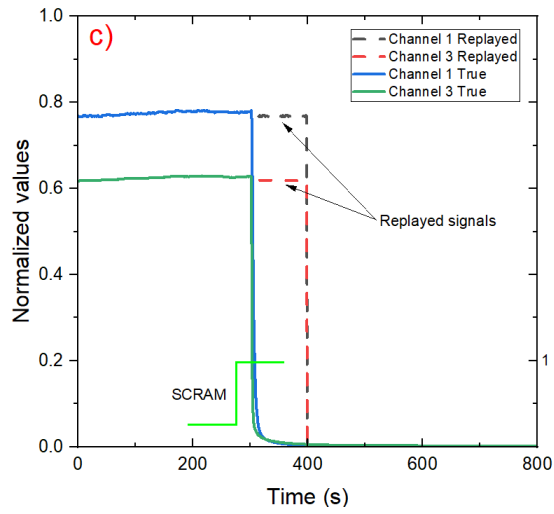
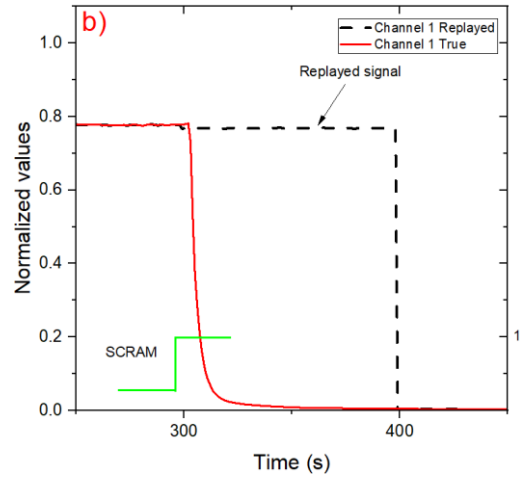
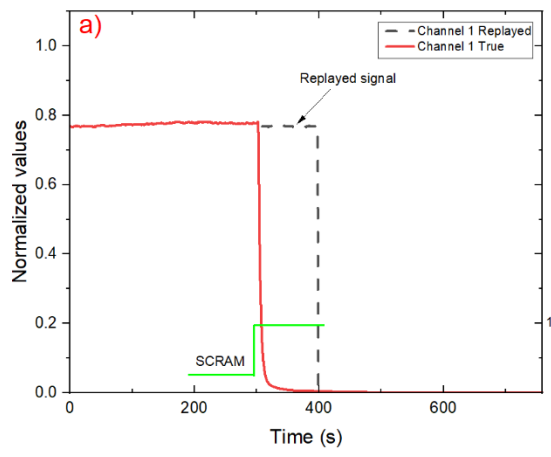


Figure 7: Expected signal behavior during a SCRAM event

Following the process described in the scenario section, six replayed datasets were generated each involving an increasing number of falsified signals:

1. Replay#1: Replay attack of one signal (ch.1)
2. Replay#2: Replay attack of two signals (ch.1, ch.3)s
3. Replay#3: Replay attack of three signals (ch.1, ch.3, ch.4)
4. Replay#4: Replay attack of four signals (ch.1, ch.3, ch.4, rr)
5. Replay#5: Replay attack of five signals (ch.1, ch.3, ch.4, rr, SS1)
6. Replay#6: Replay attack of six signals (ch.1, ch.3, ch.4, rr, SS1, SS2)

Out of the nine signals listed in Table 1, the three control rod active states remained unchanged in all cases to allow the algorithm to detect the deviation from the normal case. Figure 8 presents the six simulated datasets. All signal values have been normalized to account for signal variability and ensure consistent visualization. Each dataset is divided into two panels: The left side displays the full 800 seconds of the SCRAM operation under the replay attack. The right side presents the same condition restricted to the critical time frame the SCRAM is happening (300-400 seconds).



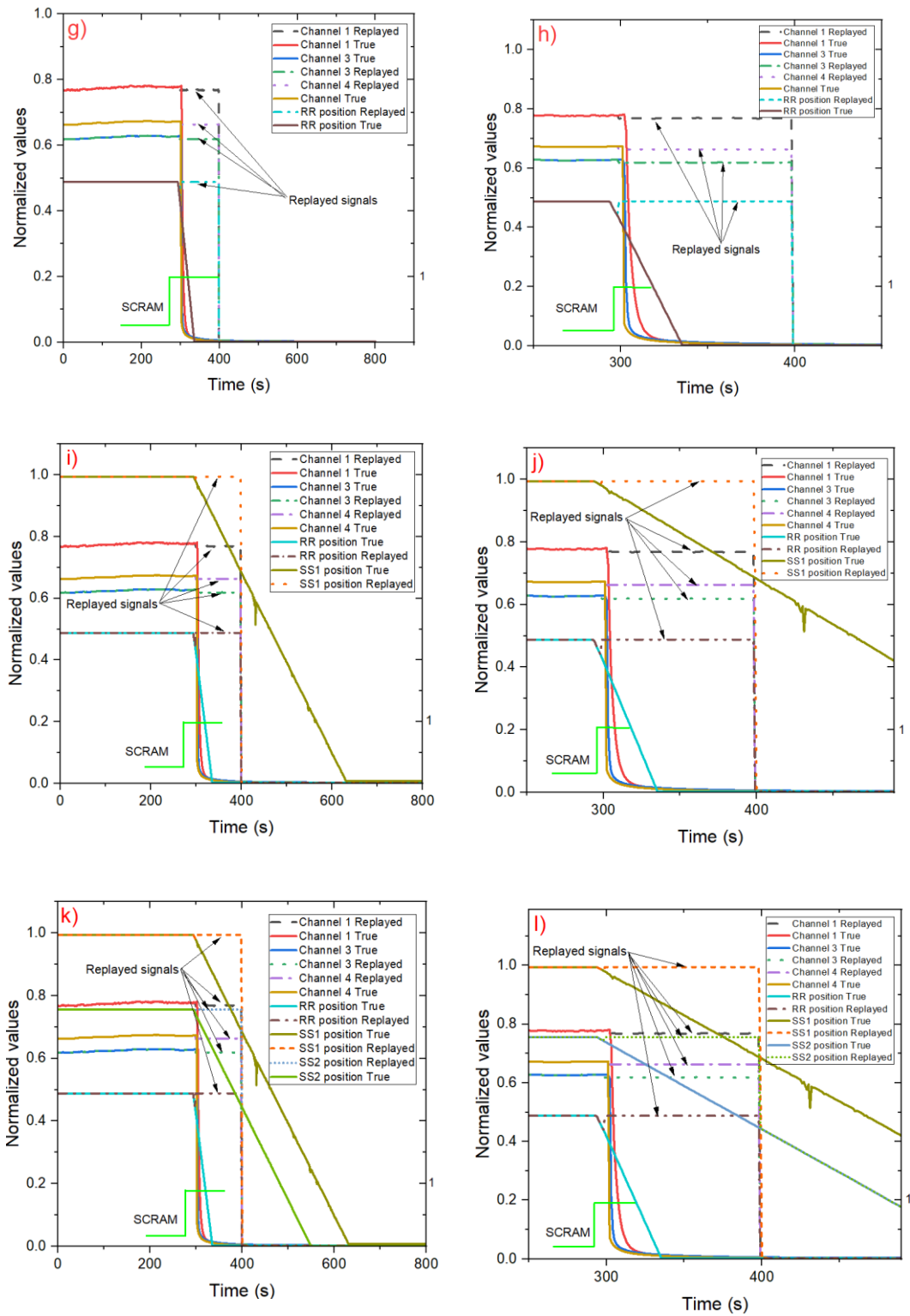


Figure 8: Replay attack one signal (a-b); Replay attack two signals (c-d); Replay attack three signals (e-f); Replay attack four signals (g-h). Replay attack five signals (i-j). Replay attack six signals (k-l). All signal values have been normalized to account for differing value ranges and facilitate visualization.

Methodology

The proposed framework consists of three modules. The first module leverages a deep AE architecture composed of layers with time sequence learning capabilities, to form a reconstructive model of PUR-1 from the nine signals in Table 1. The second module analyzes the reconstructive model by comparing it with live data and decides whether a deviation from normal expectation is in place. The third module adds local interpretability for attack type and source identification as well as duration and timing information and is based on a customized window SHAP-based approach for MTS data. The entire framework is presented in Figure 9.

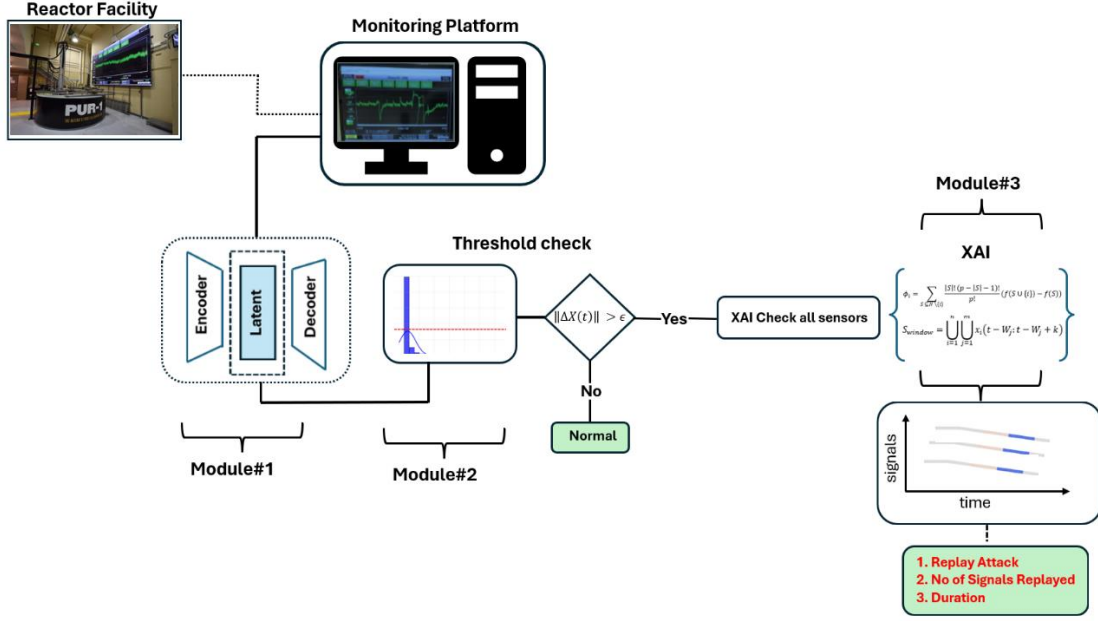


Figure 9: Methodology workflow

Module 1: Reconstructive Modeling of Reactor Behavior

The first module involves training a deep AE architecture exclusively on normal data to allow the system to learn expected reactor behavior. By using a large number of full reactor power cycles (Figure 6) a model is constructed capturing the inherent dynamics, correlations and interdependencies of sensor signals at all possible reactor conditions (startups, steady states, transients, shutdowns). The trained model learns to reconstruct signal values based on input signals. Let

$$X(t) = [x_1(t), x_2(t), \dots, x_n(t)] \quad t \in I$$

represent the set of n sensor measurements at a time interval I , where $x_i(t)$ is the reading from the i -th sensor. A reconstructive model f is trained under normal operational conditions on historical data to learn the functional mapping:

$$\hat{X}(t) = f(X(t))$$

Where $\hat{X}(t)$ is the model's reconstruction for the set $X(t)$ at the same time interval I . The fundamental concept is to create a lower dimensional representation of the input

time series through a sequence of neural layers and then reconstructing it back to its original dimensional space. The model is optimized by adjusting its weights and biases to minimize the error between the original and the reconstructed data for the fixed time interval I , over the entire length of the training data, such that:

$$\min_f \mathbb{E}[\|X(I) - \hat{X}(I)\|]$$

Where $\|\cdot\|$ represents a norm appropriate to quantify similarities between two given vectors like mean squared error or absolute error. To optimize the reconstruction accuracy and ensure adaptability, we explored an appropriate AE architecture capable of inferring temporal dependencies in a multisensory dynamic environment.

A number of methods have demonstrated their effectiveness in capturing temporal dependencies and anomaly detection in MTS data with characteristic examples being the Autoregressive Moving Average and its variants, correlation methods and ensemble methods [39][40][41][42][43]. Despite their success, AE architectures have gained attention and have become the standard approach for unsupervised anomaly detection due to their ability to generalize, and their robustness to noise [44]. Although not originally designed for anomaly detection, AE were introduced in the work of Rumelhart et al., 1986 [45] as a novel method for dimensionality reduction and representation learning, with applications on image storage and transmission. Their application for anomaly detection became prominent post 2010 with advancements in efficient deep learning architectures and computational units. In one of the first studies, Sakurada et al., 2014 [27] show that AE can effectively detect anomalies through nonlinear dimensionality reduction. The process involves training a mirrored network of neural layers with normal data, which enables the network to learn standard behavior of the system. At inference, deviations from this behavior are flagged as potential anomalies. In [44][46][47] unsupervised frameworks based on AE for anomaly detection and diagnosis in MTS are proposed with improved results when compared to baseline methods. Despite their performance, these methods do not consider patterns when abnormalities are flagged or are assuming simplified assumptions regarding the root diagnosis of the abnormal event and therefore are not applicable to scenarios where interpretability is required at full scale.

AE are comprised of three parts: the encoder which compresses the input data by performing dimensionality reduction, the latent representation, which adds extra layers of neurons to capture meaningful patterns in the lower dimensional data, and the decoder, which decompresses the data from the latent space to their initial dimensions. Due to the large range of applications, a number of different AE architectures have been proposed each for a specific purpose. Most significant examples include: vanilla AE, deep AE, convolutional AE, RNN-based AE, LSTM AE and Variational AE. A full taxonomy of architectures and uses can be found in this work [48]. In our study, to capture the temporal dependencies, LSTM layers [49] are employed in the design of the AE architecture. LSTM networks are well-suited for time series data due to their ability to capture long and short term temporal dependencies. The equations governing the LSTM cell at a given timestep t are:

$$\begin{aligned}
f_t &= \sigma(W_f x_t + U_f h_{t-1} + b_f) \\
i_t &= \sigma(W_i x_t + U_i h_{t-1} + b_i) \\
\tilde{c}_t &= \tanh(W_c x_t + U_c h_{t-1} + b_c) \\
c_t &= f_t \odot c_{t-1} + i_t \odot \tilde{c}_t \\
o_t &= \sigma(W_o x_t + U_o h_{t-1} + b_o) \\
h_t &= o_t \odot \tanh(c_t)
\end{aligned}$$

Where f_t is the forget gate, i_t is the input gate, \tilde{c}_t is the candidate cell, c_t is the update cell, o_t is the output cell, h_t is the final hidden state, σ is the activation function, $W_f, W_i, W_c, W_o, U_f, U_i, U_c, U_o$ are the weights matrices and b_f, b_i, b_c, b_o are the bias terms. Unlike traditional neural networks or RNNs, LSTMs are designed to retain information over long and short range dependencies, making them ideal for modeling control systems with time-dependent patterns such as reactor conditions.

Module 2: Reconstruction Error Analysis

The second module involves analyzing the errors of the reconstructive model from module 1 as a quantitative measurement for potential anomalies in the system. An advantage of using AE architecture in the first module is that AE are trained exclusively on normal operational data, eliminating the need to obtain hard to find anomalies. Additionally, the use of AE enables the detection of previously unseen anomalies without prior knowledge of what the data represents, eliminating the need to manually label known irregularities in the system. Reconstruction error analysis has been successfully demonstrated in relevant studies. This study [50] presents an efficient AE methodology to predict potential anomalies in the cooling system of a simulated PWR, based on the reconstruction error between new unseen data and trained data. Similar studies in the nuclear domain include [51], [52], [53] where the large value in the reconstruction error indicates a potential anomaly for their specific cases.

The main difference in our study is that the anomaly does not represent an obvious trend as time advances, but rather the lack of signal intercorrelation at a specific dynamic condition which is ultimately driven by reactor operation. In this context, the replay attack has a conceptual effect which only a trained operator with knowledge over the system can identify. The replay attack becomes effective once the data deviate significantly from the true condition, affecting the decision-making process which potentially may lead to unsafe reactor operation. To identify the replay attack first a metric which will trigger a flag at a given time is required. Let's assume a modified measurement vector:

$$\tilde{X}(t) = [\tilde{x}_1(t), \tilde{x}_2(t), \dots, \tilde{x}_n(t)]$$

where $\tilde{x}_i(t)$ represents the replayed value of the i -th sensor at time t . The deviation introduced by the replay attack is given by:

$$\Delta X(t) = \tilde{X}(t) - X(t)$$

Where $X(t)$ is the reconstructed data of $\tilde{X}(t)$ at time t . An anomaly is flagged for a potential replay attack if:

$$\|\Delta X(t)\| > \epsilon, \quad \forall t \in I$$

Where I is a fixed time interval within the time series, and ϵ is the minimum deviation required to cause the system's response. To identify the threshold ϵ , we employed different window lengths as part of the hyperparameter tuning in the training data. Module 2 continuously evaluates the residual errors at the predefined window over the entire time series. Sections of the time series that fall below the threshold are considered normal reactor operation, while for the sequence that falls above the error a post hoc interpretability is employed to analyze whether patterns are in place that justify a replay attack.

Module 3: Source and Timing Identification with Post Hoc Explainability

In module 2 the system identifies a condition which deviates from the normal pattern based on the reconstruction error at a t -window sequence at a time t . Detecting a deviation alone does not confirm a replay attack and certainly does not identify the source, as deviations can arise from a number of other factors such as operational changes, noise in the system or sensor malfunction. In this module, we introduce a modified SHAP analysis optimized for MTS data to add a layer of explainability and investigate the source of falsified sensors and the duration of the attack.

While AE and other AI/ML algorithms have been successfully used in data driven applications in a variety of different engineering and industrial problems [26], their lack of explainability, especially in considering multi signal monitoring and human-scale explanation, complicates their adaption in critical infrastructure [54]. Moreover, research conducted in [55] [56] has shown that lack of trust in advanced data analytics techniques can be attributed to the difficulty of gaining clear insights from such models. To fill this gap, SHAP analysis has emerged recently from game theory as a model agnostic framework designed to explain ML predictions [57] [58]. The framework quantifies feature contributions to the prediction of any ML model by assigning Shapley values to each feature, which either offset or support the prediction. SHAP was initially introduced to provide global explanations, as the models were becoming more complex the focus shifted towards instance-specific explanations [27]. In our study, we emphasize the need for time sequence level explanation, in cases where the underlying system dynamics change over time.

The Shapley value for a given feature i is:

$$\phi_i = \sum_{S \subseteq N \setminus \{i\}} \frac{|S|! (p - |S| - 1)!}{p!} (f(S \cup \{i\}) - f(S))$$

Where, ϕ_i represents the Shapley value calculated for feature i , p is the total numbers of features in the dataset, S is all possible subsets (or coalitions) of features that don't include i , $|S|$ represents the number of features in subset S , and $f(S \cup \{i\}) - f(S)$ is the marginal contribution of feature i to subset S . The summation runs over all possible subsets S of features, excluding feature i . The function $f(S)$ is defined as:

$$f(S) = \int f(x_1, \dots, x_p) dP_{x \notin S} - E(f(X))$$

where $f(x_1, \dots, x_p)$ is the model's prediction over all features in S , $dP_{x \notin S}$ is the marginal distribution over the features not present in S (missing features). The integral term accounts for the expected model output by averaging over all possible values of the missing features, based on their marginal distribution. $E(f(X))$, represents the expected value of the model's output on the full feature vector, which serves as the baseline reference. The sum of all Shapley values ϕ_i is equal to the difference between the model's output and the expected output at the baseline $E(f(X))$. Each individual value represents the contribution of the specific feature to this difference.

Implementation

Data processing

The datasets used for training were preprocessed to ensure they were appropriately formatted for input to an AE model. The first step involves collecting the data from the monitoring software of the digital twin system (Figure 3), either in real time while the reactor is in operation, or at a later time by identifying reactor operation time periods. Each dataset was normalized using a Min-Max scaler to a range between 0 and 1. To ensure consistent scaling across all datasets, the minimum and maximum values for each feature were derived from the last 3 years of reactor operation. During training each dataset representing a distinct reactor operation, are converted on the fly into 3D tensors which are fed to the AE model. The tensors are constructed by sliding a window one second at a time across the dataset, regardless of its length as shown in Figure 10. This process generates tensors of dimensions (batch size x window length x features). This format is well suited when training MTS data, as it ensures that during testing the model consistently considers the past window seconds at each time step and reconstructs the same window length for further analysis. The optimal window length was found to be 10 seconds.

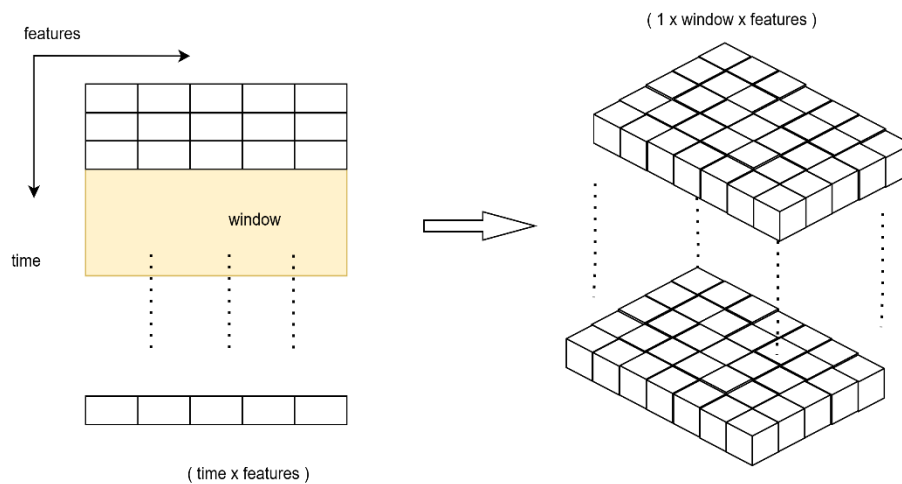


Figure 10: Tensors created for training by sliding a window one second at each step. This creates (data length-window) tensors of dimensions (1 x window size x features)

Training, tuning, implementation

We trained the AE model initially on the full cycles data to allow the model to learn the reactor dynamics, followed by transfer learning on the SCRAM dataset to refine the detection of changes under sudden and extreme signal variability. To optimize the AE architecture, hyperparameter tuning was performed using Bayesian optimization [59]. Hyperparameter tuning is considered a necessary step in any ML application, as the choice of hyperparameters highly affects the model’s performance [60]. Bayesian optimization was chosen among other common methods (e.g. grid search, random search, etc.) due to the noisy nature of the data, the depth of the architecture employed, and its ability to select the next hyperparameters based on prior results.

The AE architecture is designed to be flexible in hyperparameter tuning. The different choices include the depth and the width of the LSTM layers, across the encoder, the decoder, and the latent representation. The search space includes a range of values for the hidden layers, the possible units per layer, the batch size, the dropout regularization to reduce the overfitting, and the learning rate. Table 2 shows the optimal set of hyperparameters found through tuning. Out of the 47 datasets of the full reactor cycles, 34 datasets were used for the training during hyperparameter optimization, 10 were used for the validation, and the remaining 3 were used for testing after the hyperparameter tuning was completed. The tuner evaluated 20 different hyperparameters combinations from the predefined search space, with each model trained for 30 epochs. The criterion for the optimal selection was to minimize the Mean Squared Error (MSE) on the validation loss. The optimal architecture is presented in Table 2 and Figure 11. Figure 12 presents the training and the validation loss during training for the optimal architecture.

Table 2: Optimal Hyperparameters for the AE architecture

Hyperparameter	
Learning Rate	0.000352
Encoder Hidden Layer #1	256 neurons
Dropout Layer	0.1
Encoder Hidden Layer #2	128 neurons
bottleneck	32 neurons
Decoder Hidden Layer #1	128 neurons
Dropout Layer	0.2
Decoder Hidden Layer #2	128 neurons
Batch size	32
Window size	10

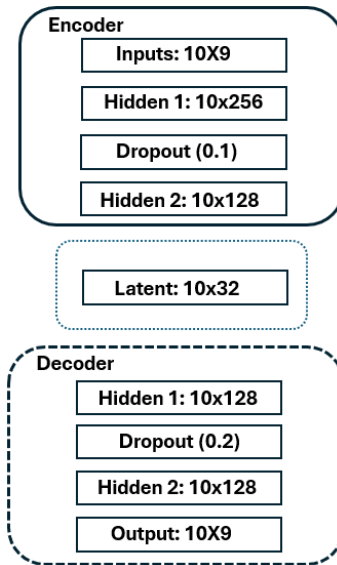


Figure 11: Structure diagram for the AE architecture

A Python package, called Nuclear-replay-attack-detection, accompanies this paper. It is publicly available at <https://github.com/Kvasili/Nuclear-replay-attack-detection> and it comes with an example of running the proposed framework on the data used to simulate the replayed attacks. The training, testing and tuning make use of Tensorflow, Keras, sklearn, and Pandas libraries. Simulations were run on an NVIDIA GeForce GTX 1650 Ti, with a training time of approximately 4 hours for 30 epochs on the full cycle datasets.

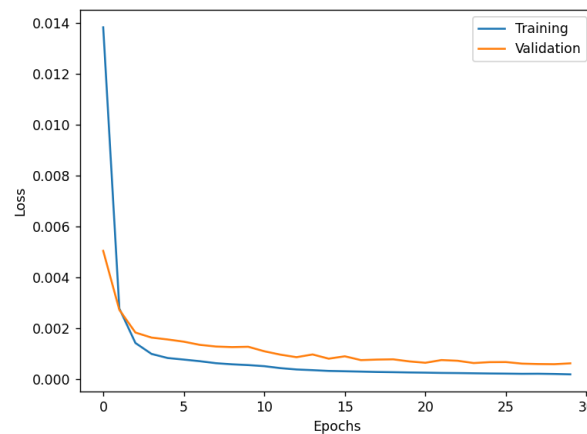


Figure 12: Training validation loss for the optimized architecture on the full cycle dataset

To gain an understanding of the model's performance on new unseen data, the trained network was applied to the 3 testing datasets. Figure 13 shows a comparison between the reconstructed and the original data for the neutron counts of the testing dataset. The model is able to reconstruct adequately the signal, proving that the reconstructive modeling of reactor behavior is successfully addressed. During steady state the model consistently returns very low errors, while spikes are observed when reactor conditions change, especially during startup and shutdown where transients take place. This means that during those events a disagreement between the model and the actual behavior may

lead to high reconstruction errors, which in turn will allow the identification of potential anomalies.

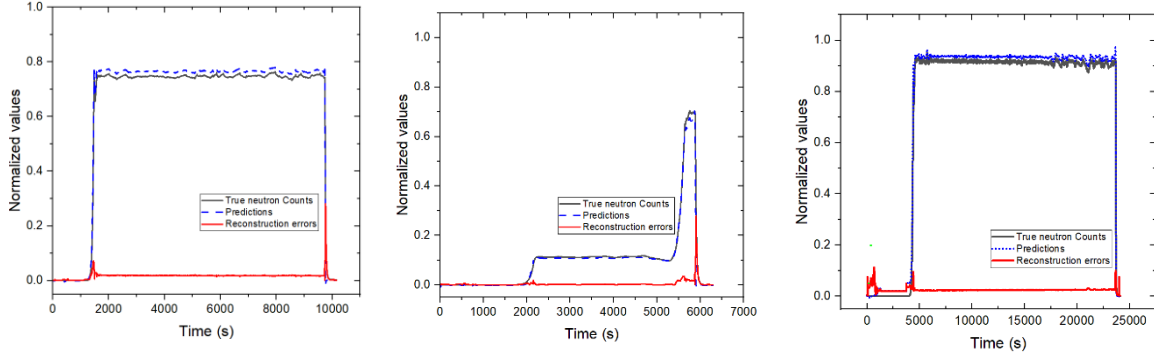


Figure 13: Reactor reconstructive modeling on the testing dataset

Fine tuning on the SCRAM dataset

Errors produced by training the models with the full cycle, showed that this is not adequate to fully adjust to the reactor dynamics during the extreme signal variability of a SCRAM process. Furthermore, the limited number of SCRAM events alone is estimated to affect the performance of the models to detect attacks under this process. To solve this problem the optimized network was used for further tuning on the SCRAM dataset. As described, the dataset consists of 24 events of roughly 800 seconds in which the SCRAM duration is reflected in the signals between 300 and 400 seconds (Figure 7). Following the same network architecture and hyperparameters defined during tuning, and the same logic in preprocessing the data, the model was further trained. This process fine tunes the network's weights and biases to the dynamics of the SCRAM process, enhancing its ability to detect any deviations from expected patterns when exposed to falsified or erroneous data. Out of the 24 datasets, 20 were used for the training and 4 for the validation. The steps described in the last two sections represent the reconstructive modeling of reactor behavior of our methodology.

Reconstruction error analysis

This step serves as the implementation of the second module in our methodology. The model's loss objective function is to minimize the reconstruction errors of the sequence representing the normal operation during training, in order to accurately reconstruct the normal features and inaccurately reconstruct the anomalous features during testing. Anomalies can be detected by evaluating the magnitude of either the MSE or the MAE given by the following formulas respectively:

$$MSE = \frac{1}{N} \sum (X - X')^2$$

$$MAE = \frac{1}{N} \sum |X - X'|$$

Where N is the number of the samples in the training set, representing the number of tensors created. X is the vector containing the sensor values at a specific window and X' is the vector with the predicted values. Following the logic applied in relevant studies [50] [55] [56], the threshold to define an anomaly is determined by the distribution of MSE or MAE on the normal data. Observing the distribution one can understand how well the model is able to reconstruct the sequences and can define a threshold above which a sequence is identified as a non normal pattern. Figures 14.a and 14.b show the reconstruction error distribution by calculating the MAE on the data sequences for the training and the validation datasets. To investigate the performance, we also provide the error distribution in one of the falsified datasets that simulate the replay attack. The visualization reveals almost identical, skewed to the left, normal distributions for both the training and the validation datasets, with the vast majority of the reconstructed sequences located close to the zero bin. This indicates the network’s success in reconstructing and predicting accurate values. Error values are also observed in the range larger than 0.2, but with a much smaller frequency of appearance. These values can be explained by the noise inherent in the system or other sensor artifacts. As a sample result, Figure 14c presents the error distribution on an unseen falsified dataset, as if the analysis was to be performed after the attack. The pattern differs significantly from the distribution in the normal datasets. Although there is a large concentration of errors in the small value bins, which falls into the statistical uncertainty of the normal datasets, a significant concentration of large errors is also observed around the 0.4 bin. This suggests that a portion of the sequences clearly deviates from the expected behavior and therefore a potential anomaly is present in the system.

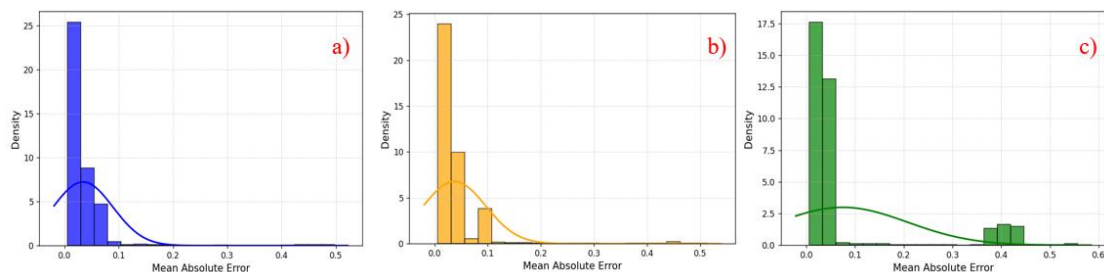


Figure 14: Reconstruction error distributions for training (a), validation (b), and testing (c) datasets

XAI implementation

SHAP analysis was initially introduced as a model agnostic approach to provide general interpretability for any ML model predictions [57] [58]. Applying SHAP directly to MTS data leads to an increased computational cost, as it would require the estimation of Shapley values over all combinations of feature-time datapoints. To overcome this shortcoming, a windowSHAP approach was proposed in this study [61], which restricts the calculation to distinct temporal windows. This approach reduces the complexity while preserving interpretability when explanations are required in a specific time sequence. The general formula is:

$$S_{window} = \bigcup_{i=1}^n \bigcup_{j=1}^m x_i(t - W_j: t - W_j + k)$$

Where \cup represents the union across all features and windows, x_i is the i -th feature in the MTS, W_j is the offset for the j -th window, k is the window size, and $x_i(t - W_j: t - W_j + k)$ is a sequence of the feature x_i . In practice this formula calculates Shapley values per window, identifying the timesteps and features within that window that have the most influence on the model's output.

For our case, the proposed approach needed to be modified to account for the specifics of the AE, and the dynamics of the critical event in the reactor system. WindowSHAP occludes data by replacing the “missing” values from a defined subwindow with the global average. This would not work well for this use case, because occluded values are meant to represent a baseline and expected behavior of the feature. In contrast, most periods of reactor operation are at a power level sufficiently far from the mean, and an instant change in power back to the global mean would not represent an expected baseline reactor behavior. To accurately describe the baseline condition during a SCRAM event, the baseline condition was set as the expected signal behavior for all the signals in the dataset during the event (Figure 15) and is dynamically updated over time to account for the signal variability as the event evolves. This way importance is attributed to the features whose evolution over the input time window causes the greatest change in error.

The interpretation of Shapley values is highly affected by the selection of the baseline data. Negative Shapley values indicate that the change in a certain feature is decreasing the error, indicating a correlation with the predicted signal, positive Shapley values indicate that the change in an input feature is increasing the error, indicating a lack of correlation with the predicted signal. Shapley values near zero indicate that the signal is at the baseline or that the variation in a signal from the baseline did not influence the error. By applying the modified WindowSHAP as long as the reconstruction error is triggered, a pattern is observed in the case of a replay attack in the Shapley values of each feature, which is an indicator to distinguish this specific abnormality from other types like FDI or sensor malfunctions. This is less computationally expensive than the distance profile matrix methods used in relevant studies, where a comparison is made between the current flagged sequence will all the possible sequences in the past time.

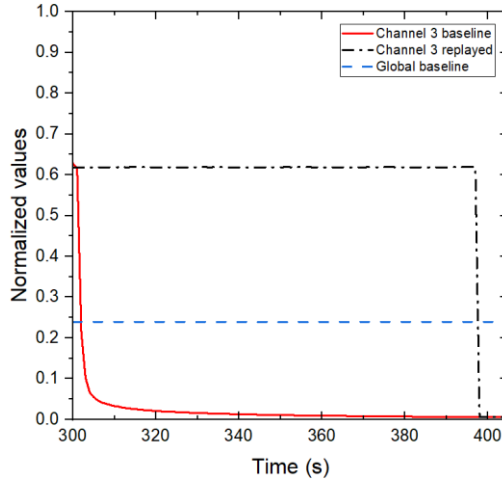


Figure 15: Comparison between replayed, expected behavior, and the global mean baseline for reactor power during the SCRAM event.

Results

To detect anomalies effectively, we first need to determine the appropriate threshold that triggers the detection of a deviation from the normal patterns. We analyze the error second by step by evaluating the reconstruction error at a sliding window of 10 seconds. For each time step, the model computes the reconstruction error over the preceding 10-second window, and an anomaly is flagged if this error exceeds a defined threshold. Comparing the flagged anomaly with the true label, an anomaly detection metric is determined, which shows the percentage of time steps in each dataset exceeding the error threshold. Table 3 shows the results for varying error threshold between 0.05 and 0.25 for each of the datasets. The optimal error threshold normally would be determined by validating only the normal dataset, since in a real time scenario the abnormal data are not known. However, to assess the AE ability to capture anomalies, results are shown for both normal and abnormal datasets. From Table 3, for an error threshold between 0.1 and 0.2 the accuracy falls inside the range 93-98% for the Normal dataset. Setting the threshold at 0.15 returns a detection accuracy more than 96% across all datasets.

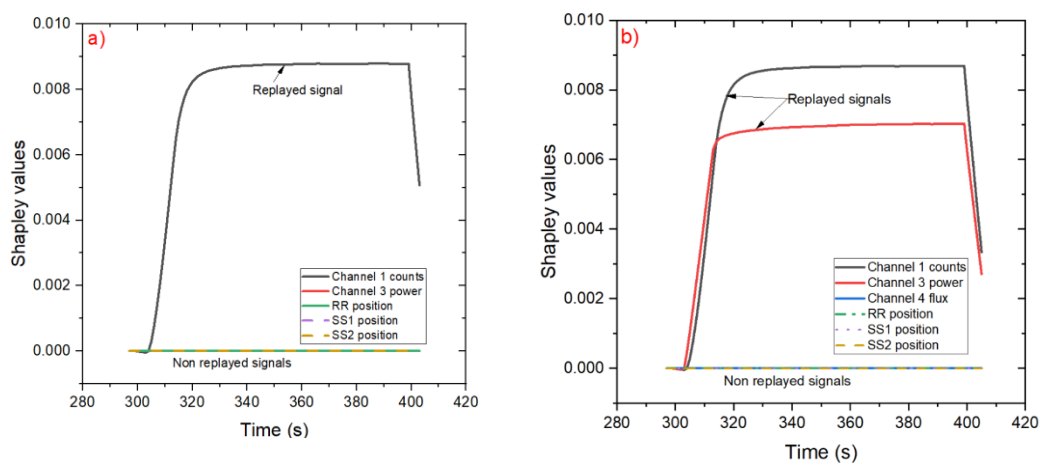
Table 3: Detection accuracy as a function of the error threshold

Threshold	Normal	Replay#1	Replay#2	Replay#3	Replay#4	Replay#5	Replay#6
0.05	0.65	0.77	0.77	0.77	0.77	0.77	0.77
0.1	0.93	0.97	0.97	0.97	0.97	0.97	0.97
0.11	0.94	0.97	0.97	0.97	0.97	0.97	0.97
0.12	0.95	0.96	0.97	0.97	0.97	0.97	0.97
0.13	0.95	0.96	0.97	0.97	0.97	0.97	0.97
0.14	0.96	0.96	0.97	0.97	0.97	0.97	0.97
0.15	0.97	0.96	0.97	0.97	0.97	0.98	0.98
0.2	0.98	0.88	0.97	0.98	0.97	0.98	0.98
0.25	0.98	0.86	0.91	0.98	0.98	0.98	0.98

Even though the AE architecture can effectively identify deviations from normal reactor behavior, this does not guarantee that an identified anomaly is a replay attack. Time windows which exceed the threshold are passed to the XAI module for further analysis.

The XAI module is using the modified windowSHAP algorithm to evaluate the contribution of each feature at each time step on the reconstruction error of the flagged window. More specifically each Shapley value represents the contribution of each signal to the difference between the reconstruction error of the flagged window and the reconstruction error by replacing the baseline behavior for each signal. A negative Shapley value for signal x at time t , indicates that this portion of the signal is correlated with the expected signal behavior found in the baseline (Figure 15) since it tends to lower the error. A positive value indicates that the signal x at the time t , deviates from the baseline behavior since it tends to increase the error. A value close to zero indicates an agreement with the baseline. The signals which exceed the error threshold in module 2 were presented to the XAI module and the Shapley values in each 10 second window are averaged, to provide a single value per second per signal/feature.

A pattern emerges from analyzing the Shapley values in the replayed datasets. Figure 16 shows the Shapley values when the error exceeds the threshold, which correctly happens during the falsification of the signals in all 6 cases. For the three signals measuring neutron counts (ch.1), reactor power (ch.3), and neutron flux (ch.4), the Shapley values begin from zero and linearly increase for the first 15 seconds, indicating a linearly increasing disagreement between the expected behavior, which should be dropping rapidly, and the replayed signal. For the next 60 seconds Shapley values present a repeated pattern indicating similar behavior of disagreement between the repeated and the expected signal, which now have been stabilized to small values. Finally, once the attack ends after 100 seconds, the Shapley values drop rapidly until nearly zero, indicating a decreasing disagreement until the attack is over and the signals obtain their expected value. The pattern is similar in all cases, which means that the same type of attack is present with an increasing number of signals in each case. In all cases the expected values are drawn from the baseline signals.



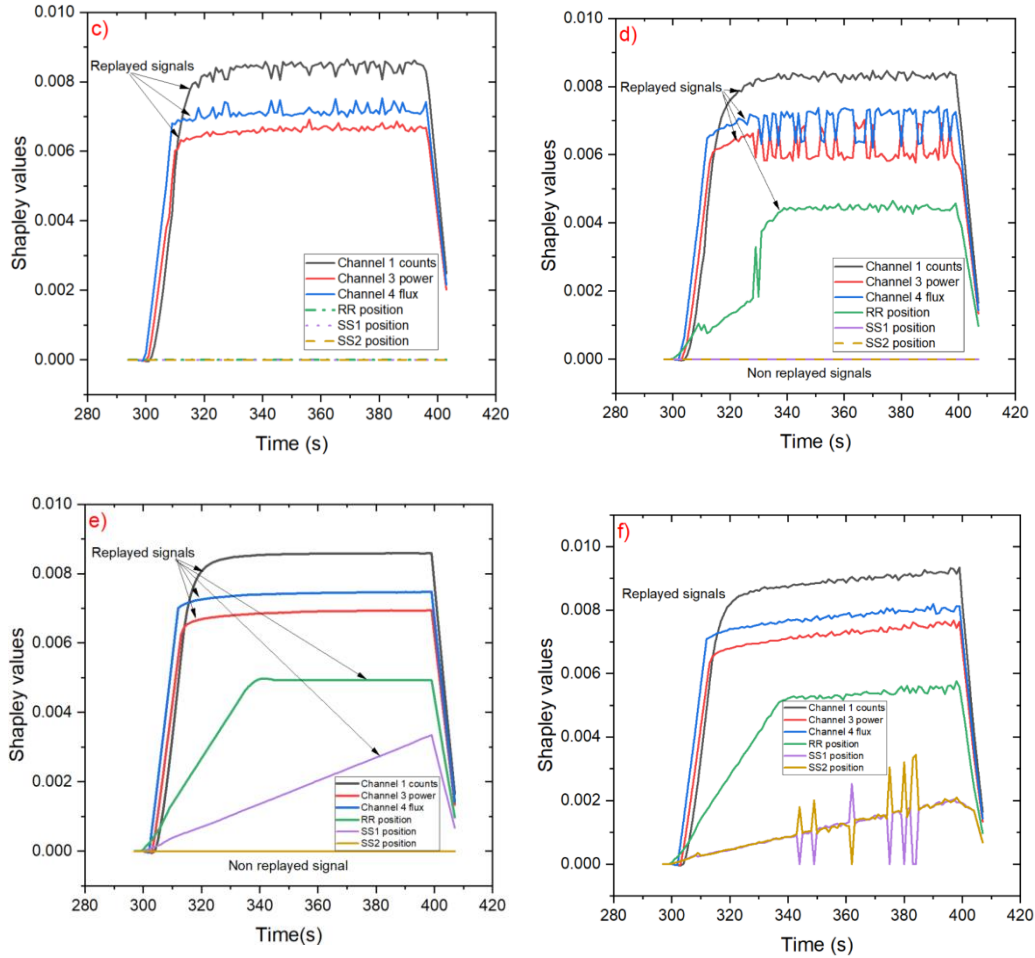


Figure 16: Shapley values per second per feature for the duration of the attack for a) Replay#1 b) Replay#2 c) Replay#3 d) Replay#4 e) Replay#5 f) Replay#6.

For the three signals measuring the control rod positions, a similar pattern is observed. The rr rod (green line in Figure 16d-e-f) during the SCRAM event is rapidly inserted into the core, while the falsified signal maintains steady values for the entire duration. Shapley values show a near linear disagreement for the first 30 seconds, which matches the time needed for the rr rod drivers to show the effect. Then, the Shapley values are steady showing a steady disagreement between the actual signal, which now is fully inserted, and the high values in the replayed signal. For the last few seconds, the shapley values drop quickly and linearly because the signals are back to their normal values at the end of the attack. For the SS1 and SS2 rods, the Shapley values (purple and yellow line in Figure 16 e-f) show a linear and increasing disagreement almost for the entire duration of the attack, which matches the behavior of the steady replayed signals and the actual signals which are dropping linearly, until a few seconds before the attack where the Shapley values drop rapidly indicating the end of the attack. Although the general trend is linear, some spikes are observed in the SS1 and SS2 Shapley values for the last case (Figure 16f), which can be attributed to the noise of the signals. As observed, increasing the number of falsified signals results in smaller Shapley values for each new signal at each time step. This is attributed to the distribution of the reconstruction error difference across a larger number of signals, where the most

influential signals contribute more significantly to the overall error deviation between the falsified signals and the baseline. Lastly, the repeated patterns observed in the extracted Shapley values across all the falsified signals, are a direct result of the repeated nature of the replay attack. In the case of a different falsification (e.g. an FDI attack), the Shapley values are expected to have different patterns and interpretation. This distinction supports the conclusion that the detected intrusion corresponds to a replay attack.

Figures 17-22 present the visualization of the above logic in real time. The signals are presented to the framework second by second, and every 10 seconds the reconstruction error is calculated for the current window, which is visualized with green, if it falls inside the normal pattern, or red otherwise. In case an abnormality is flagged, the XAI module is activated to analyze the pattern and identify the falsified signals which are highlighted in red. At the end, the duration of the replayed signals along with the number of signals that have been replayed are presented. Table 4 presents the percentage of the signals which are correctly identified as replayed per dataset. Frame f) in each Figure displays the final set of detected replayed signals correctly ranging from one signal to six signals replayed. Frame c) presents a case where despite the AE flagging an anomaly, the SHAP analysis does not indicate a disagreement with the expected signal behavior. This occurs just when the SCRAM process begins where the signals' variability is not yet seen, thus a clear pattern (normal or abnormal) is not yet established. After the first 10 seconds, when the patterns begin to emerge, the SHAP analysis consistently succeeds in identifying the replayed signals across all cases. Also in frame f, across all cases the falsified signals seem to be extended for approximately 10 seconds after the attack. This can be attributed to the framework's use of a 10 second window, where the average Shapley value across the window is used to characterize each second. As a result, even if only one high value exists while the others are zero, the window may still be flagged as abnormal and replayed. The effect quickly vanishes when the entire window presents no high Shapley values, as seen right after the attack is over in frames f.

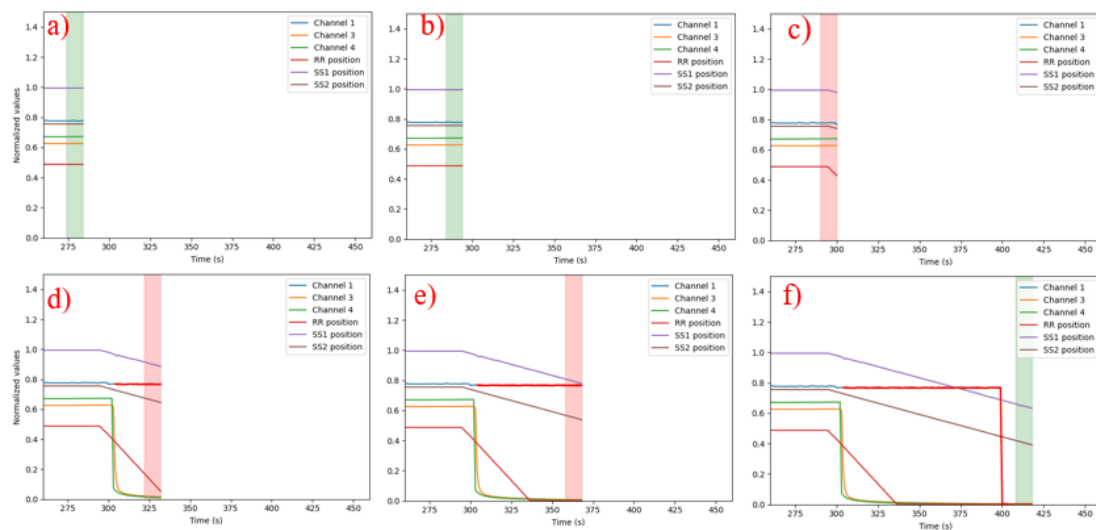


Figure 17: Replay attack detection for Replay#1 dataset

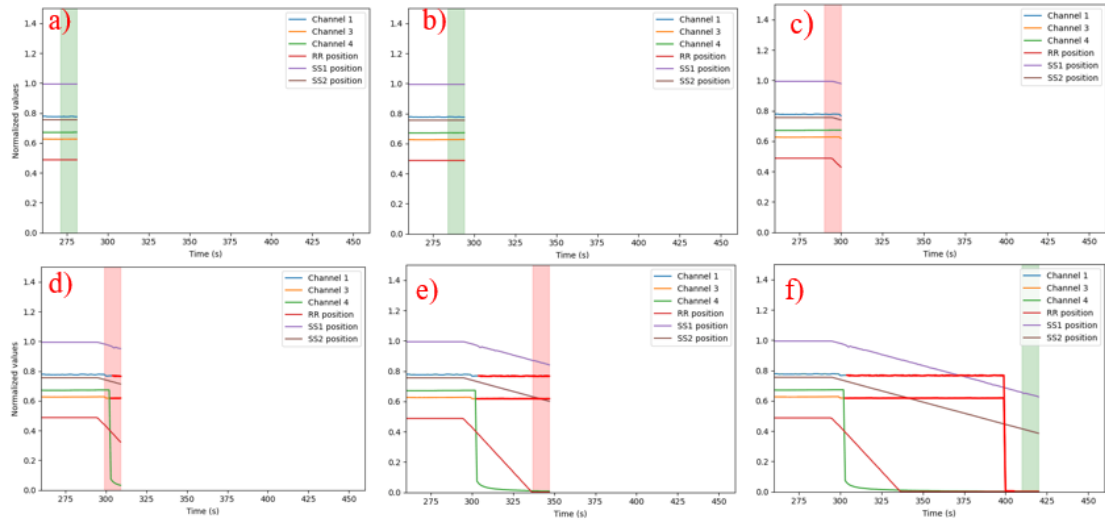


Figure 18: Replay attack detection for Replay#2 dataset

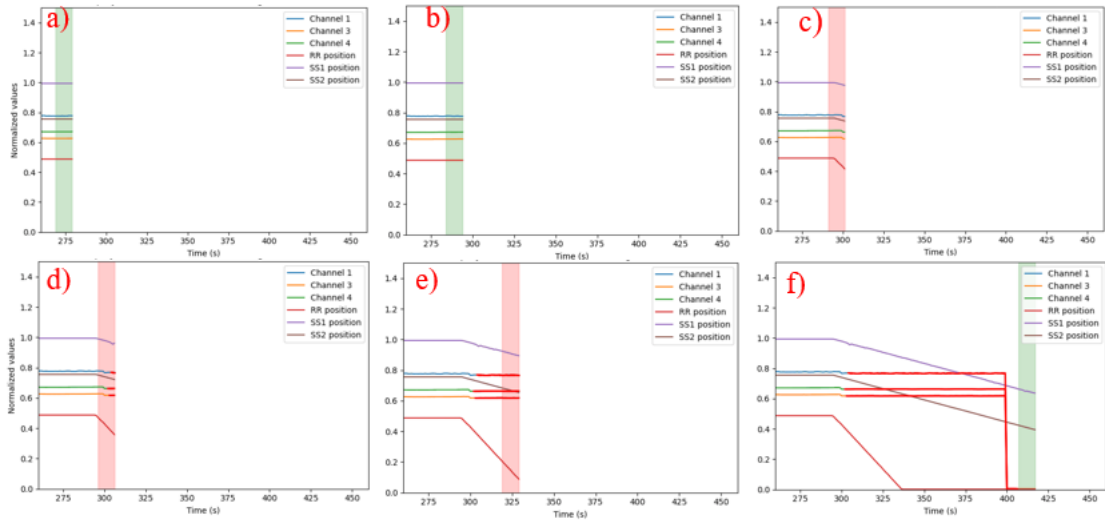


Figure 19: Replay attack detection for Replay#3 dataset

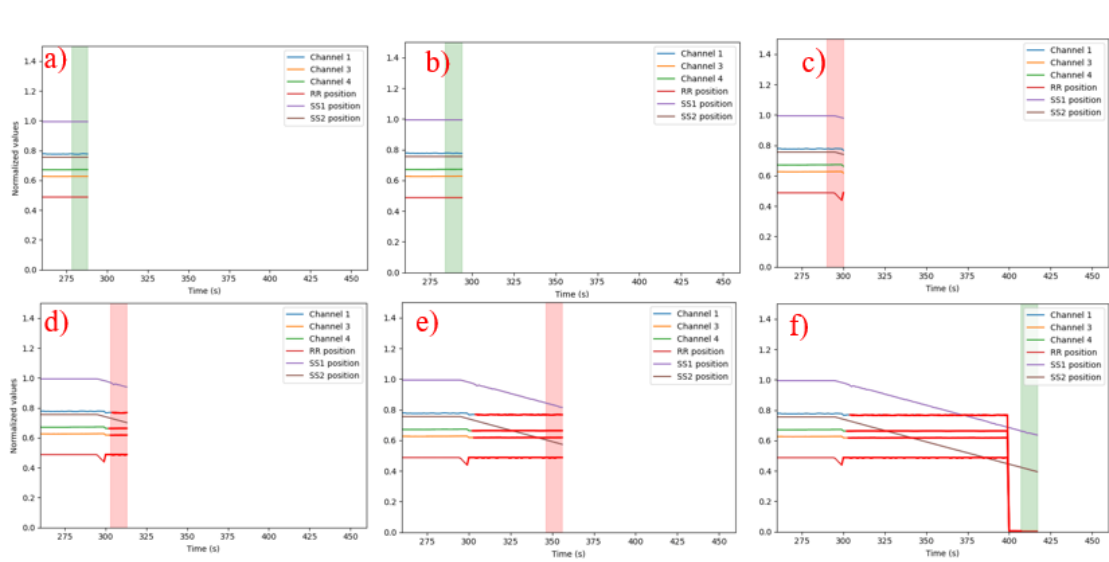


Figure 20: Replay attack detection for Replay#4 dataset

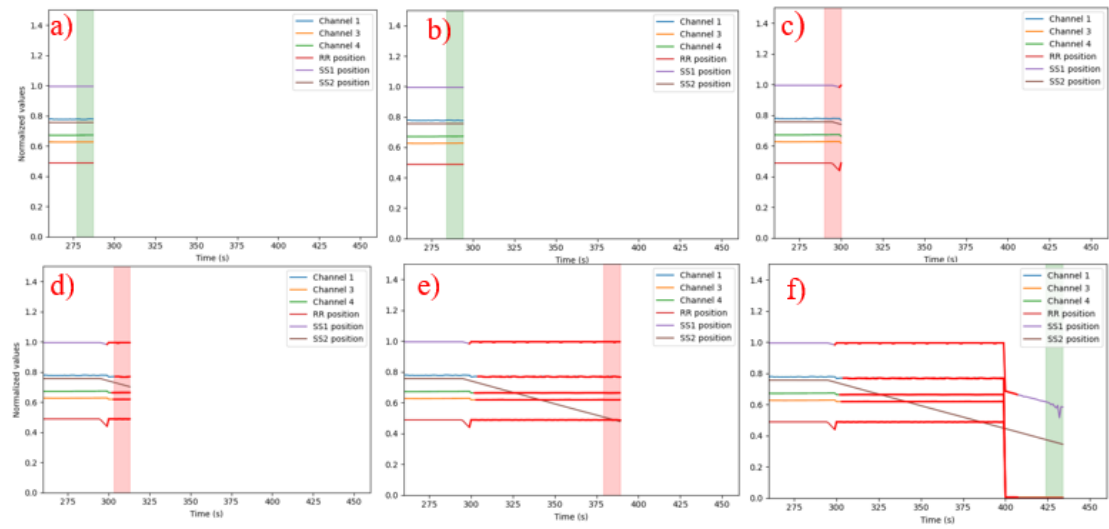


Figure 21: Replay attack detection for Replay#5 dataset

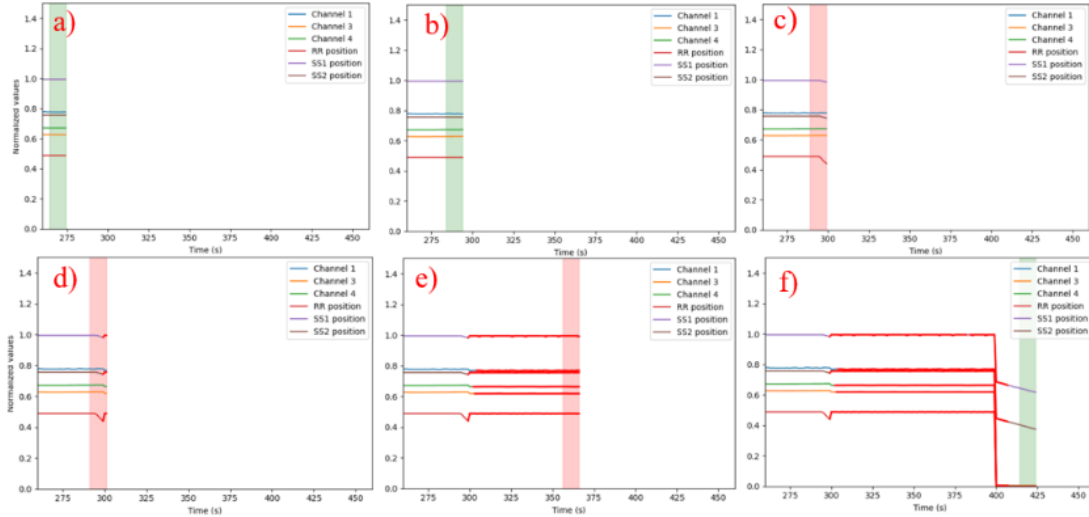


Figure 22: Replay attack detection for Replay#6 dataset

Table 4: Percentage of each dataset accurately identified as replayed

	Accuracy					
	Replay#1	Replay#2	Replay#3	Replay#4	Replay#5	Replay#6
Channel 1	95%	95%	95%	95%	95%	95%
Channel 3		96%	96%	96%	96%	96%
Channel 4			97%	97%	97%	97%
RR				99%	99%	99%
SS1					99%	99%
SS2						99%

Conclusions

In this work, we propose a replay attack detection and localization framework that integrates an optimized deep AE architecture for nuclear MTS data, with a modified XAI module based on a windowSHAP algorithm. The network is trained solely on normal reactor data, eliminating the need to manually label and define training classes. We focus on a dynamic and time evolving usecase of reactor operation to simulate the attack, with an increasing number of falsified signals ranging from one up to six concurrent signals. The results show success in triggering an abnormality and identifying the number of replayed signals as well as the duration of the falsification in each signal within a single unified framework.

Although the framework was benchmarked on real-world datasets from PUR-1, it is estimated that it can be applicable to a wide range of practical scenarios where the expected signal behavior is known and can be used as a reference. Potential applications may include sensor drift detection, trajectory correction, and anomaly detection in

multisensory environments. It is not our intention to distinguish in depth between a replay attack and other abnormalities that seemingly may have the same effect e.g. a sensor malfunction, because the problem has adequately been addressed in relevant studies by using rule-based methods [22] or matrix-based profile methods [20] for a single sensor. Rather, we provide an effective and robust approach to the problem of a sophisticated multisensory anomaly detection scenario under a time evolving reactor operation, where the expected dynamics are known. Moving forward, we understand that post hoc explanations can have caveats in terms of computational cost. As future work we aim to investigate the extent to which the number of falsified signals is affecting the performance in real time settings, and we intend to assess the framework's generalizability in other anomaly detection tasks.

Acknowledgements

This research was performed using funding received from the DOE Office of Nuclear Energy's Nuclear Energy University Program under contract DE-NE0009268.

References

- [1] L. Lin *et al.*, "Development and assessment of a nearly autonomous management and control system for advanced reactors," *Ann. Nucl. Energy*, vol. 150, p. 107861, Jan. 2021, doi: 10.1016/j.anucene.2020.107861.
- [2] R. T. Wood, B. R. Upadhyaya, and D. C. Floyd, "An autonomous control framework for advanced reactors," *Nucl. Eng. Technol.*, vol. 49, no. 5, pp. 896–904, Aug. 2017, doi: 10.1016/j.net.2017.07.001.
- [3] S. M. Cetiner *et al.*, "Supervisory Control System for Multi-Modular Advanced Reactors," Oak Ridge National Laboratory (ORNL), Oak Ridge, TN (United States), ORNL/TM-2016/693, Nov. 2016. doi: 10.2172/1615832.
- [4] K. Gkouliaras, V. Theos, Z. Dahm, W. Richards, K. Vasili, and S. Chatzidakis, "False Data Injection Detection in Nuclear Systems Using Dynamic Noise Analysis," *IEEE Access*, vol. 12, pp. 94936–94949, 2024, doi: 10.1109/ACCESS.2024.3425270.
- [5] R. Appiah *et al.*, "Development of a Cloud-based Application to Enable a Scalable Risk-informed Predictive Maintenance Strategy at Nuclear Power Plants," Idaho National Laboratory (INL), Idaho Falls, ID (United States), INL/RPT-22-70543-Rev000, Dec. 2022. doi: 10.2172/1906501.
- [6] A. Teixeira, D. Pérez, H. Sandberg, and K. H. Johansson, "Attack models and scenarios for networked control systems," in *Proceedings of the 1st international conference on High Confidence Networked Systems*, in HiCoNS '12. New York, NY, USA: Association for Computing Machinery, Apr. 2012, pp. 55–64. doi: 10.1145/2185505.2185515.
- [7] "Industrial Control Systems: Cyberattack trends and countermeasures - ScienceDirect." Accessed: May 22, 2025. [Online]. Available: https://www.sciencedirect.com/science/article/pii/S0140366419319991?casa_token=twkMU9ykgwIAAAAA:sH8FKeMQ-lkkDkhf5popVKkrTpTYII33MXoW25jTaKzLkiGZlsf-4uhwgC4e-3wEWXr-c8EVFwM

- [8] M. Baezner and P. Robin, “Stuxnet,” ETH Zurich, Oct. 2017. doi: 10.3929/ETHZ-B-000200661.
- [9] J. P. Farwell and R. Rohozinski, “Stuxnet and the Future of Cyber War,” *Survival*, Feb. 2011, Accessed: May 22, 2025. [Online]. Available: <https://www.tandfonline.com/doi/abs/10.1080/00396338.2011.555586>
- [10] “Research Challenges for the Security of Control Systems.” Accessed: May 16, 2025. [Online]. Available: https://www.usenix.org/legacy/event/hotsec08/tech/full_papers/cardenas/cardenas_html/
- [11] S. Amin, A. A. Cárdenas, and S. S. Sastry, “Safe and Secure Networked Control Systems under Denial-of-Service Attacks,” in *Hybrid Systems: Computation and Control*, R. Majumdar and P. Tabuada, Eds., Berlin, Heidelberg: Springer, 2009, pp. 31–45. doi: 10.1007/978-3-642-00602-9_3.
- [12] O. Kosut, L. Jia, R. J. Thomas, and L. Tong, “Malicious Data Attacks on Smart Grid State Estimation: Attack Strategies and Countermeasures,” in *2010 First IEEE International Conference on Smart Grid Communications*, Oct. 2010, pp. 220–225. doi: 10.1109/SMARTGRID.2010.5622045.
- [13] Y. Liu, P. Ning, and M. K. Reiter, “False data injection attacks against state estimation in electric power grids,” *ACM Trans Inf Syst Secur*, vol. 14, no. 1, p. 13:1-13:33, Jun. 2011, doi: 10.1145/1952982.1952995.
- [14] Y. Mo and B. Sinopoli, “Secure control against replay attacks,” in *2009 47th Annual Allerton Conference on Communication, Control, and Computing (Allerton)*, Sep. 2009, pp. 911–918. doi: 10.1109/ALLERTON.2009.5394956.
- [15] Y. Zhao and C. Smidts, “A control-theoretic approach to detecting and distinguishing replay attacks from other anomalies in nuclear power plants,” *Prog. Nucl. Energy*, vol. 123, p. 103315, May 2020, doi: 10.1016/j.pnucene.2020.103315.
- [16] G. Liang, J. Zhao, F. Luo, S. R. Weller, and Z. Y. Dong, “A Review of False Data Injection Attacks Against Modern Power Systems,” *IEEE Trans. Smart Grid*, vol. 8, no. 4, pp. 1630–1638, Jul. 2017, doi: 10.1109/TSG.2015.2495133.
- [17] “An Event-Triggered Watermarking Strategy for Detection of Replay Attacks,” *IFAC-Pap.*, vol. 55, no. 6, pp. 317–322, Jan. 2022, doi: 10.1016/j.ifacol.2022.07.148.
- [18] J. Li, Z. Wang, Y. Shen, and L. Xie, “Attack Detection for Cyber-Physical Systems: A Zonotopic Approach,” *IEEE Trans. Autom. Control*, vol. 68, no. 11, pp. 6828–6835, Nov. 2023, doi: 10.1109/TAC.2023.3240383.
- [19] A. A. Elsaedy, N. Jagannath, A. G. Sanchis, A. Jamalipour, and K. S. Munasinghe, “Replay Attack Detection in Smart Cities Using Deep Learning,” *IEEE Access*, vol. 8, pp. 137825–137837, 2020, doi: 10.1109/ACCESS.2020.3012411.
- [20] S. Gargoum, N. Yassaie, A. W. Al-Dabbagh, and C. Feng, “A Data-Driven Framework for Verified Detection of Replay Attacks on Industrial Control Systems,” *IEEE Trans. Autom. Sci. Eng.*, vol. 22, pp. 3400–3415, 2025, doi: 10.1109/TASE.2024.3394315.
- [21] W. Wang, Y. Xie, L. Ren, X. Zhu, R. Chang, and Q. Yin, “Detection of data injection attack in industrial control system using long short term memory recurrent neural network,” in *2018 13th IEEE Conference on Industrial Electronics and Applications (ICIEA)*, May 2018, pp. 2710–2715. doi: 10.1109/ICIEA.2018.8398169.

- [22] Z. Dahm, V. Theos, K. Vasili, W. Richards, K. Gkouliaras, and S. Chatzidakis, “A One-Class Explainable Ai Framework for Identification of Non-Stationary Concurrent False Data Injections in Nuclear Reactor Signals,” Apr. 15, 2025, *Social Science Research Network, Rochester, NY*: 5217433. doi: 10.2139/ssrn.5217433.
- [23] I. Kiss, B. Genge, and P. Haller, “A clustering-based approach to detect cyber attacks in process control systems,” in *2015 IEEE 13th International Conference on Industrial Informatics (INDIN)*, Jul. 2015, pp. 142–148. doi: 10.1109/INDIN.2015.7281725.
- [24] R. Kumar, R. R. Hossain, S. Talukder, A. Jena, and A. T. A. Ghazo, “Recursive Histogram Tracking-Based Rapid Online Anomaly Detection in Cyber-Physical Systems,” *IEEE Trans. Syst. Man Cybern. Syst.*, vol. 52, no. 11, pp. 7123–7133, Nov. 2022, doi: 10.1109/TSMC.2022.3150304.
- [25] M. Ma, P. Zhou, D. Du, C. Peng, M. Fei, and H. M. AlBuflasa, “Detecting Replay Attacks in Power Systems: A Data-Driven Approach,” in *Advanced Computational Methods in Energy, Power, Electric Vehicles, and Their Integration*, K. Li, Y. Xue, S. Cui, Q. Niu, Z. Yang, and P. Luk, Eds., Singapore: Springer, 2017, pp. 450–457. doi: 10.1007/978-981-10-6364-0_45.
- [26] Z. Zamanzadeh Darban, G. I. Webb, S. Pan, C. Aggarwal, and M. Salehi, “Deep Learning for Time Series Anomaly Detection: A Survey,” *ACM Comput. Surv.*, vol. 57, no. 1, pp. 1–42, Jan. 2025, doi: 10.1145/3691338.
- [27] L. Antwarg, R. M. Miller, B. Shapira, and L. Rokach, “Explaining anomalies detected by autoencoders using Shapley Additive Explanations,” *Expert Syst. Appl.*, vol. 186, p. 115736, Dec. 2021, doi: 10.1016/j.eswa.2021.115736.
- [28] J. H. Park, H. S. Jo, S. H. Lee, S. W. Oh, and M. G. Na, “A reliable intelligent diagnostic assistant for nuclear power plants using explainable artificial intelligence of GRU-AE, LightGBM and SHAP,” *Nucl. Eng. Technol.*, vol. 54, no. 4, pp. 1271–1287, Apr. 2022, doi: 10.1016/j.net.2021.10.024.
- [29] L. Antwarg, R. M. Miller, B. Shapira, and L. Rokach, “Explaining Anomalies Detected by Autoencoders Using SHAP,” Jun. 30, 2020, *arXiv*: arXiv:1903.02407. doi: 10.48550/arXiv.1903.02407.
- [30] “Novel fault diagnosis scheme utilizing deep learning networks,” *Prog. Nucl. Energy*, vol. 118, p. 103066, Jan. 2020, doi: 10.1016/j.pnucene.2019.103066.
- [31] J. Yang and J. Kim, “An accident diagnosis algorithm using long short-term memory,” *Nucl. Eng. Technol.*, vol. 50, no. 4, Art. no. 4, May 2018, doi: 10.1016/j.net.2018.03.010.
- [32] M. C. dos Santos *et al.*, “Deep rectifier neural network applied to the accident identification problem in a PWR nuclear power plant,” *Ann. Nucl. Energy*, vol. 133, pp. 400–408, Nov. 2019, doi: 10.1016/j.anucene.2019.05.039.
- [33] H. A. Saeed, H. Wang, M. Peng, A. Hussain, and A. Nawaz, “Online fault monitoring based on deep neural network & sliding window technique,” *Prog. Nucl. Energy*, vol. 121, p. 103236, Mar. 2020, doi: 10.1016/j.pnucene.2019.103236.
- [34] J. Park, T. Kim, and S. Seong, “Providing support to operators for monitoring safety functions using reinforcement learning,” *Prog. Nucl. Energy*, vol. 118, p. 103123, Jan. 2020, doi: 10.1016/j.pnucene.2019.103123.
- [35] “Reactor,” Nuclear Engineering - Purdue University. Accessed: Jun. 04, 2025. [Online]. Available: <https://engineering.purdue.edu/NE/research/facilities/reactor>
- [36] S. Chatzidakis *et al.*, “Characterizing Nuclear Cybersecurity States Using Artificial Intelligence/Machine Learning - Final Report”.

- [37] V. Theos, K. Gkouliaras, and S. Chatzidakis, “Development and Analysis of a Real-time Digital Twin System in PUR-1,” *Proc. Nucl. Plant Instrum. Control Hum.-Mach. Interface Technol. NPIC/MIT 2025 Chic. IL June 15-18 2025*, pp. 464–473, Jun. 2025, doi: doi.org/10.13182/NPIC/MIT25-46907.
- [38] “A Distributed Cyber-Attack Detection Scheme With Application to DC Microgrids.” Accessed: Jun. 10, 2025. [Online]. Available: <https://ieeexplore.ieee.org/abstract/document/9054955>
- [39] R. B. Magadum, S. Bilagi, S. Bhandarkar, A. Patil, and A. Joshi, “Short-Term Wind Power Forecast Using Time Series Analysis: Auto-regressive Moving-average Model (ARMA),” in *Recent Developments in Electrical and Electronics Engineering*, P. Singhal, S. Kalra, B. Singh, and R. C. Bansal, Eds., Singapore: Springer Nature, 2023, pp. 319–341. doi: 10.1007/978-981-19-7993-4_26.
- [40] Q. Yu, L. Jibin, and L. Jiang, “An Improved ARIMA-Based Traffic Anomaly Detection Algorithm for Wireless Sensor Networks,” *Int. J. Distrib. Sens. Netw.*, vol. 12, no. 1, p. 9653230, Jan. 2016, doi: 10.1155/2016/9653230.
- [41] “CorrCorr: A feature selection method for multivariate correlation network anomaly detection techniques,” *Comput. Secur.*, vol. 83, pp. 234–245, Jun. 2019, doi: 10.1016/j.cose.2019.02.008.
- [42] Z. Jadidi, S. Pal, M. Hussain, and K. Nguyen Thanh, “Correlation-Based Anomaly Detection in Industrial Control Systems,” *Sensors*, vol. 23, no. 3, Art. no. 3, Jan. 2023, doi: 10.3390/s23031561.
- [43] A. Iliopoulos, J. Violos, C. Diou, and I. Varlamis, “Detection of Anomalies in Multivariate Time Series Using Ensemble Techniques,” in *2023 IEEE Ninth International Conference on Big Data Computing Service and Applications (BigDataService)*, Jul. 2023, pp. 1–8. doi: 10.1109/BigDataService58306.2023.00007.
- [44] C. Zhang *et al.*, “A Deep Neural Network for Unsupervised Anomaly Detection and Diagnosis in Multivariate Time Series Data,” *Proc. AAAI Conf. Artif. Intell.*, vol. 33, no. 01, pp. 1409–1416, Jul. 2019, doi: 10.1609/aaai.v33i01.33011409.
- [45] D. E. Rumelhart, G. E. Hinton, and R. J. Williams, “Learning representations by back-propagating errors,” *Nature*, vol. 323, no. 6088, pp. 533–536, Oct. 1986, doi: 10.1038/323533a0.
- [46] Tayeh, Tareq, “An attention-based ConvLSTM autoencoder with dynamic thresholding for unsupervised anomaly detection in multivariate time series.”
- [47] Y. Choi, H. Lim, H. Choi, and I.-J. Kim, “GAN-Based Anomaly Detection and Localization of Multivariate Time Series Data for Power Plant,” in *2020 IEEE International Conference on Big Data and Smart Computing (BigComp)*, Feb. 2020, pp. 71–74. doi: 10.1109/BigComp48618.2020.00-97.
- [48] K. Pawar and V. Z. Attar, “Assessment of Autoencoder Architectures for Data Representation,” in *Deep Learning: Concepts and Architectures*, W. Pedrycz and S.-M. Chen, Eds., Cham: Springer International Publishing, 2020, pp. 101–132. doi: 10.1007/978-3-030-31756-0_4.
- [49] S. Hochreiter and J. Schmidhuber, “Long Short-Term Memory,” *Neural Comput.*, vol. 9, no. 8, pp. 1735–1780, Nov. 1997, doi: 10.1162/neco.1997.9.8.1735.
- [50] “Unsupervised anomaly detection in pressurized water reactor digital twins using autoencoder neural networks,” *Nucl. Eng. Des.*, vol. 413, p. 112502, Nov. 2023, doi: 10.1016/j.nucengdes.2023.112502.

- [51] “Development of deep autoencoder-based anomaly detection system for HANARO,” *Nucl. Eng. Technol.*, vol. 55, no. 2, pp. 475–483, Feb. 2023, doi: 10.1016/j.net.2022.10.009.
- [52] P. Mena, R. A. Borrelli, and L. Kerby, “Detecting Anomalies in Simulated Nuclear Data Using Autoencoders,” *Nucl. Technol.*, Jan. 2024, Accessed: Jun. 13, 2025. [Online]. Available: <https://www.tandfonline.com/doi/abs/10.1080/00295450.2023.2214257>
- [53] D. Hu, C. Zhang, T. Yang, and G. Chen, “Anomaly Detection of Power Plant Equipment Using Long Short-Term Memory Based Autoencoder Neural Network,” *Sensors*, vol. 20, no. 21, Art. no. 21, Jan. 2020, doi: 10.3390/s20216164.
- [54] L. Lin, C. Walker, and V. Agarwal, “Explainable machine-learning tools for predictive maintenance of circulating water systems in nuclear power plants,” *Nucl. Eng. Technol.*, vol. 57, no. 9, p. 103588, Sep. 2025, doi: 10.1016/j.net.2025.103588.
- [55] A. Barredo Arrieta *et al.*, “Explainable Artificial Intelligence (XAI): Concepts, taxonomies, opportunities and challenges toward responsible AI,” *Inf. Fusion*, vol. 58, pp. 82–115, Jun. 2020, doi: 10.1016/j.inffus.2019.12.012.
- [56] O. Fink, Q. Wang, M. Svensén, P. Dersin, W.-J. Lee, and M. Ducoffe, “Potential, challenges and future directions for deep learning in prognostics and health management applications,” *Eng. Appl. Artif. Intell.*, vol. 92, p. 103678, Jun. 2020, doi: 10.1016/j.engappai.2020.103678.
- [57] S. M. Lundberg and S.-I. Lee, “A Unified Approach to Interpreting Model Predictions,” in *Advances in Neural Information Processing Systems*, Curran Associates, Inc., 2017. Accessed: Jun. 03, 2025. [Online]. Available: https://proceedings.neurips.cc/paper_files/paper/2017/hash/8a20a8621978632d76c43dfd28b67767-Abstract.html
- [58] “Lundberg: Consistent individualized feature attribution... - Google Scholar.” Accessed: Jun. 04, 2025. [Online]. Available: https://scholar.google.com/scholar_lookup?title=Consistent%20Individualized%20Feature%20Attribution%20for%20Tree%20Ensembles&author=S.M.%20Lundberg&publication_year=2018
- [59] T. T. Joy, S. Rana, S. Gupta, and S. Venkatesh, “Hyperparameter tuning for big data using Bayesian optimisation,” in *2016 23rd International Conference on Pattern Recognition (ICPR)*, Dec. 2016, pp. 2574–2579. doi: 10.1109/ICPR.2016.7900023.
- [60] L. Yang and A. Shami, “On hyperparameter optimization of machine learning algorithms: Theory and practice,” *Neurocomputing*, vol. 415, pp. 295–316, Nov. 2020, doi: 10.1016/j.neucom.2020.07.061.
- [61] A. Nayebi, S. Tipirneni, C. K. Reddy, B. Foreman, and V. Subbian, “WindowSHAP: An Efficient Framework for Explaining Time-series Classifiers based on Shapley Values,” May 08, 2023, *arXiv*: arXiv:2211.06507. doi: 10.48550/arXiv.2211.06507.